RSC Advances

PAPER

Atomically precise and monolayer protected iridium clusters in solution†

Shridevi Bhat,[a] Indranath Chakraborty,‡[a] Tuhina Adit Maark,[ab] Anuradha Mitra,[c] Goutam De[c] and Thalappil Pradeep*[a]

The first atomically precise and monolayer protected iridium cluster in solution, $Ir_9(PET)_6$ (PET − 2-phenyethanethiol) was synthesized *via* a solid state method. The absence of a plasmonic band at ∼350 nm, expected in the UV/Vis spectra for spherical Ir particles of 10 nm size indicated that the synthesized cluster is smaller than this dimension. Small angle X-ray scattering (SAXS) showed that the cluster has a particle size of ∼2 nm in solution which was confirmed by transmission electron microscopy (TEM). The blue emission of the cluster is much weaker than many noble metal clusters investigated so far. X-ray photoelectron spectroscopy (XPS) measurements showed that all Ir atoms of the cluster are close to the zero oxidation state. The characteristic S−H vibrational peak of PET at 2560 cm^{-1} was absent in the FT-IR spectrum of the cluster indicating RS−Ir bond formation. The molecular formula of the cluster, $Ir_9(PET)_6$ was assigned based on the most significant peak at m/z 2553 in the matrix assisted laser desorption ionization mass spectrum (MALDI MS), measured at the threshold laser intensity. Density functional theory calculations on small $Ir@SCH_3$ and $Ir@PET$ clusters and comparison of the predictions with the IR and ^{1}H-NMR spectra of $Ir_9(PET)_6$ suggested that the PET ligands have two distinct structural arrangements and are likely to be present as bridging thiolates −(Ir−SR−Ir)− and singly attached thiolates −(Ir−SR).

1. Introduction

Sub-nanometer sized monolayer-protected clusters (MPCs) or nanoclusters of noble metals exhibiting molecule-like behavior, have gained tremendous importance during the past few years, due to their unique physical and chemical properties and promising applications.[1] Considerable theoretical and experimental developments have been made in this field, enriching our understanding of this new class of materials.[2] Thiolate-protected noble metal nanoparticles, first synthesized by Brust and Schiffrin in 1994,[3] form a major sub-group of these materials. The synthesis of atomically precise clusters in this category can be traced back to the early work of Murray and Whetten, although clusters of the type Au_{11}, Au_{13} and Au_{55} were known for quite some time.[4]

Gold and silver MPCs and their alloys have been investigated to a large extent and a number of reports exist on their synthetic methodologies, structure, properties and applications in various fields.[5–8] Many gold clusters like Au_{23}, Au_{24}, Au_{25}, Au_{28}, Au_{30}, Au_{36}, Au_{38} and Au_{102} protected by ligands such as phenylethanethiol (PET), mercaptobenzoic acid (MBA), *etc.*, have been crystallized and their structures have been studied by X-ray crystallography.[5] Apart from these, a number of other gold MPCs have been synthesized and characterized, though their crystal structures are unknown.[9] In comparison with gold MPCs, the literature on silver MPCs is limited because of their high reactivity.[10] However, several silver MPCs like $Ag_7(SR)_7$, $Ag_8(SR)_8$, $Ag_9(SR)_7$, $Ag_{32}(SR)_{19}$, $Ag_{44}(SeR)_{30}$, and $Ag_{152}(SR)_{60}$, *etc.*, have been synthesized and their properties have been studied.[6,11,12] The crystal structures of silver MPCs like $Ag_{14}(SC_6H_3F_2)_{12}(PPh_3)_8$ (PPh_3 − triphenylphosphine), $Ag_{16}(DPPE)_4(SPhF_2)_{14}$ [DPPE − 1,2-bis(diphenylphospheno)ethane], $[PPh_4]_2[Ag_{32}(DPPE)_5(SPhCF_3)_{24}]$, $Na_4Ag_{44}(p\text{-MBA})_{30}$ have been determined.[5] Recently, $Ag_{25}(SR)_{18}$ cluster has been crystallized and its structure was determined to be similar to that of $Au_{25}(SR)_{18}$ cluster.[13] Some of the alloy clusters like $Au_{24}Hg_1(SR)_{18}$,[14] $Au_{24}Cd_1(SR)_{18}$,[15] *etc.*, have been characterized by single crystal XRD and efforts are on-going to crystallize many more MPCs and obtain their structures using X-ray crystallographic techniques.

Besides Au and Ag MPCs, synthesis of MPCs of metals like Cu, Pt, and Pd is being attempted around the globe using different templates and various preparative methods, but

[a]DST Unit of Nanoscience (DST UNS) and Thematic Unit of Excellence, Department of Chemistry, Indian Institute of Technology Madras, Chennai 600036, India. E-mail: pradeep@iitm.ac.in

[b]Department of Physics, Indian Institute of Technology Madras, Chennai 600036, India

[c]CSIR-Central Glass and Ceramic Research Institute, Kolkata 700032, West Bengal, India

‡ Current address: University of Illinois at Urbana Champaign, Urbana, IL 61801, USA.

significant success has not been achieved in this regard. For instance, only a few studies are reported on copper MPCs protected by different ligands such as DNA,[16] proteins like bovine serum albumin (BSA),[17] lysozyme,[18] benzotriazolate[19] and thiols.[20] Certain luminescent Pt MPCs with capping agents such as dendrimers like poly(amidoamine) (PAMAM),[21] polymers,[22] glutathione[23] and 4-(*tert*-butyl)benzyl mercapton (BBSH)[24] are now known. Some MPCs of Pd[25,26] have also been synthesized and examined for their catalytic properties. However, relative to Au and Ag MPCs, the number of reports on other noble metal MPCs is very small.

Iridium is one of the noble metals, interesting due to its catalytic and electrocatalytic activities. Its complexes are also well known for their catalytic properties. It is one of the most efficient catalysts for C–C bond hydrogenolysis[27] and is also commonly used to facilitate the reduction of imines to the corresponding amines.[28]

As early as in 1994, Xu *et al.* investigated bare Ir$_4$ and Ir$_6$ clusters on porous metal oxide supports for hydrogenation reactions of hydrocarbons and found that the two clusters exhibited different catalytic activities, which were also dissimilar to those of metallic Ir in bulk.[29] In 1998, Berko and Solymosi carried out a scanning tunnelling microscopic study of Ir nanoparticles produced on TiO$_2$(110)-(1 × 2) surface.[30] Very high reactivity of supported Ir nanoparticles of size 1–3 nm towards CO was demonstrated by this study; whereas larger nanoparticles of size 8–10 nm did not show this behavior. Through a spectroscopic investigation, Argo *et al.* have shown that the rate of hydrogenation of ethene is several times faster on Ir$_4$ cluster than on Ir$_6$ cluster, when these clusters are supported on γ-Al$_2$O$_3$.[31] The authors have also studied hydrogenation of propene and toluene and elucidated the patterns of reactivity as a function of reactant size and structure.[32] Ir$_6$ clusters in zeolite super cages have been imaged directly using aberration corrected scanning electron microscopy by Aydin *et al.*[33] This study was the first example wherein high-dose electron beam was applied to image a metal cluster on a nanoporous material. They have also characterized the catalytic activity of these clusters for ethene hydrogenation reaction.[33] Rueping and co-workers have developed a hydrogenolytic method for the synthesis of Ir nanoparticles supported on carbon nanotubes.[28] Kerpal *et al.* used infrared multiple photon dissociation spectroscopic technique to study the adsorption of CO on neutral Ir clusters of size ranging from 3 to 21 atoms.[34] Garcia-Cuello *et al.* studied the catalytic activity of Ir nanocatalysts confined in mesoporous silica SBA-15 (Santa Barbara Amorphous type material) in CO oxidation reaction.[35]

There exist some reports on the synthesis and catalysis of colloidal Ir particles as well. To quote some, Ir nanoparticle synthesis using imidazolium ionic liquid has been tried and the catalytic activity of these nanoparticles in hydrogenation reactions has been reported.[36,37] Bayram *et al.* studied the *in situ* formation of "weakly ligated/labile ligand" Ir(0) nanoparticles (*i.e.*, nanoparticles where only weakly coordinated ligands and the desired catalytic reagents are present) and their aggregates obtained from commercially available [(1,5-COD)IrCl]$_2$ at ~2.7 atm H$_2$ and at ~22 °C and checked their catalytic behavior

in benzene hydrogenation reaction at room temperature and mild pressures.[38] Octadecanethiol functionalised Ir nanoparticles of size ranging from 2–4 nm were synthesized by Yee *et al.* using superhydride as reducing agent following one phase synthesis, in THF. The resulting nanoparticles were characterized by TEM (transmission electron microscopy), FT-IR and other techniques.[39] Synthesis of Ir nanoparticles by solid-state method[40] and hydrothermal and solvothermal methods,[41,42] *etc.*, have been tried by different groups. Most recently, Vankayala *et al.* have synthesized florescent Ir clusters protected by 2,2′-binapthol and have studied their application in cellular imaging.[43] Gavia *et al.* have synthesized dodecanethiolate protected magnetic Ir nanoparticles of size around 1.2 ± 0.3 nm by employing sodium *S*-dodecylthiosulfate as a ligand precursor during modified Brust–Schiffrin reaction.[44]

Although there is large interest in case of supported Ir clusters and their catalytic properties, the research on protected nanoparticles of this metal in solution is still in its infancy. Though there are some efforts on the synthesis of such particles in solution, no report on mass spectrometric characterization of these materials and no suggestion of their atomic compositions exist in the literature. Compared with conventional metallic nanoparticle catalysts, such materials possess several advantages such as well-defined composition, unique electronic properties, *etc.*[45] Hence, it is important to develop synthetic strategies of such materials and to study their properties.

Herein, we report the solid state synthesis of an Ir cluster with 2-phenylethanethiol (PET) as the protecting agent. The absence of plasmon band at ~350 nm in the UV/Vis spectrum of the Ir@PET indicates the cluster size regime of the particles. The average core size and particle size in solution were determined by TEM and SAXS analysis, respectively. The cluster was characterized by different spectroscopic techniques like X-ray photoelectron spectroscopy (XPS), Fourier-transform infrared (FT-IR) spectroscopy, *etc.* It shows a weak emission in the blue region. The powder X-ray diffraction (XRD) pattern of the cluster also indicated the nano-size regime. This Ir@PET cluster was assigned the composition, Ir$_9$(PET)$_6$ based on matrix assisted laser desorption ionization mass spectrometry (MALDI MS). Density functional theory (DFT) calculations were performed on small Ir@SCH$_3$ and Ir@PET clusters to understand the structure of the cluster. Based on a comparison of computed IR spectra and ^{1}H NMR chemical shifts of the ligand and model clusters, it is predicted that in the synthesized Ir$_9$(PET)$_6$ cluster, the PET ligands are present in two different structural arrangements: some PET are bonded to a single Ir atom and others are shared between two bonded Ir atoms.

2. Experimental section

Chemicals

Iridium(III) chloride hydrate (IrCl$_3$·xH$_2$O), 2-phenylethanethiol (PET), sodium borohydride (NaBH$_4$), *trans*-2-[3-(4-*tert*-butylphenyl)-2-methyl-2-propenylicene malanonitrile (DCTB), 2,5-dihydroxybenzoic acid (DHB) and 2-cyano-4-hydroxy cinnamic acid (CHCA) were purchased from Sigma Aldrich.

Toluene, tetrahydrofuran (THF), dichloromethane (DCM) and methanol were purchased from Rankem.

Synthesis of $Ir_9(PET)_6$

The $Ir_9(PET)_6$ cluster was synthesized using a solid-state route.[10] This method involved three steps. In the first step, $IrCl_3 \cdot xH_2O$ and PET (in 1 : 4 molar ratio) were mixed together by grinding in a mortar and pestle for about 10–15 minutes until the mixture turned yellow, indicating the formation of Ir–PET thiolates. Then these thiolates were reduced by adding $NaBH_4$ powder (1 : 24 molar ratio of salt : reducing agent) and grinding until the mixture turned black, in ambient atmosphere. Finally, the so formed cluster was extracted in toluene. To remove excess thiolates and thiol in the mixture, first the mixture was washed with water. Then toluene was evaporated by vacuum drying in a rotavapor and the cluster was precipitated by adding excess methanol. Following centrifugation, the supernatant solution containing the soluble thiolates and thiol was discarded, leaving behind the purified precipitate. The precipitated cluster could be re-dispersed in toluene, THF or DCM.

3.   Computational details

In this work we have considered small clusters of the type: $Ir_2(SCH_3)$, $Ir_3(SCH_3)_2$, $Ir_2(PET)_1$ and $Ir_3(PET)_1$ as model systems. Several structural isomers of these systems were generated and studied. The geometries of all the structures were optimized using density functional theory (DFT) as implemented in the Gaussian 09 program package.[46] In ref. 47 the Perdew–Burke–Ernzerhof (PBE) exchange–correlation functional has been shown to perform as well as B3LYP and B3PW91 functionals to yield bond lengths and vibrational frequencies for Ir_2 and Pd_2 dimers in good agreement with experiments. PBE has also been successfully applied to study Ir and its alloy clusters previously.[48–50] Therefore, we chose to use the PBE functional in this study. The QZVP basis set was fitted to the charge density *via* the W06 fitting set of Ahlrichs and co-workers, to enhance the performance of pure DFT calculations.[51,52] The following convergence criteria were adopted for the geometry optimizations: 10^{-7} a.u. for energy, 10^{-7} a.u. for electron density, 0.00045 a.u. for force and 0.0018 a.u. for atomic displacement. Frequency calculations were carried out for all the clusters to prove that the resulting stationary points were real energy minima, without imaginary frequencies in their vibration spectra. The atomic charges of Ir@PET and Ir@SCH_3 clusters were derived using APT (Atomic Polar Tensors)[53] and Mulliken population analyses schemes, respectively. The infra-red (IR) spectra and molecular structures were generated using the visualization program, MOLDEN.[54] The NMR chemical shifts were calculated with tetramethylsilane (TMS) as reference from the magnetic shielding tensors computed with the IGAIM[55,56] method available with Gaussian 09.

4.   Results and discussion

Preliminary control experiments were performed to determine the best conditions for the synthesis of $Ir_9(PET)_6$ cluster. For this purpose, salt : thiol ratio was varied from 1 : 2 to 1 : 4 to 1 : 6. As described in the Experimental section, in each case, the product formed was first extracted in toluene. The UV/Vis spectra and the photographs of these samples (in toluene) are shown in the ESI Fig. S2.† The molar ratio of 1 : 4 yielded $Ir_9(PET)_6$ cluster with an intense color and it had absorption features different from other two compositions. Therefore, this ratio was chosen to be used in all further synthesis.

After methanol precipitation and purification, the cluster was found to be dispersible in toluene, THF, chloroform ($CHCl_3$) and DCM (CH_2Cl_2). The cluster solution in THF was greenish brown in color, as can be seen in the photograph shown in inset (i) of Fig. 1a. Inset (iii) of Fig. 1a depicts a schematic representation of the cluster. The UV/Vis spectrum of the cluster in THF is presented in Fig. 1a (red trace). It is noticeable from the figure that the onset of absorption starts around 600 nm and the spectrum has small humps, indicated by the arrows, at approximately 500 nm and 305 nm. Based on reported theoretical calculations, the plasmonic band of spherical Ir particles of 10 nm size lies at $\sim$350 nm.[57] The absence of any plasmonic peak at this position in the UV/Vis absorption spectrum is an evidence for cluster formation. In a control experiment, the synthesis was stopped on completion of the first step, *i.e.*, after grinding the precursor salt with thiol until yellow color was achieved, no further reduction with $NaBH_4$ was carried out and the formed thiolates were extracted in ethanol. The photograph of solution of Ir–PET thiolates in ethanol is shown in inset (ii) of Fig. 1a. The UV/Vis spectrum of extracted thiolates was measured and compared with that of the cluster (see Fig. 1a, black trace). Interestingly, unlike the cluster, the thiolates exhibited a sharp peak around 350 nm.

Photoluminescence of $Ir_9(PET)_6$ was also analysed. In Fig. 1b the black trace corresponds to its excitation spectrum which shows a peak at 370 nm. The emission spectrum of the cluster when excited at 370 nm is shown as the red trace in Fig. 1b. The cluster shows emission in the blue region with peaks at 404, 432 and 460 nm. Emission features with distinct structures are reminiscent of molecular systems. These emission features are however, different from the stating materials or thiolates. Inset in the figure shows photographs of the cluster under visible (left) and UV (right) irradiation. A faint blue emission is evident in these photographs as well.

Fig. 2a shows the TEM image of the $Ir_9(PET)_6$ cluster. It was obtained by drop casting a THF solution of the cluster on a carbon-coated copper grid and drying in air. As can be seen from the particle size distribution curve, shown as inset (ii) in Fig. 2a, average size of the particles is approximately 1.6 nm, although many clusters aggregated upon electron beam irradiation. The particle size distribution of the cluster solution was further investigated through transmission SAXS using 'sphere' and 'core–shell' models considering the spherical nature of the particles. In the latter case, the PET ligands were considered as shell and the metal cluster as core (see ESI†).[58,59] The size distribution curves and the corresponding fitted SAXS profiles obtained from 'sphere' and 'core–shell' models have been shown in Fig. S1† and 2b, respectively. Both the models yielded good fittings (low residual factor) and the detailed SAXS
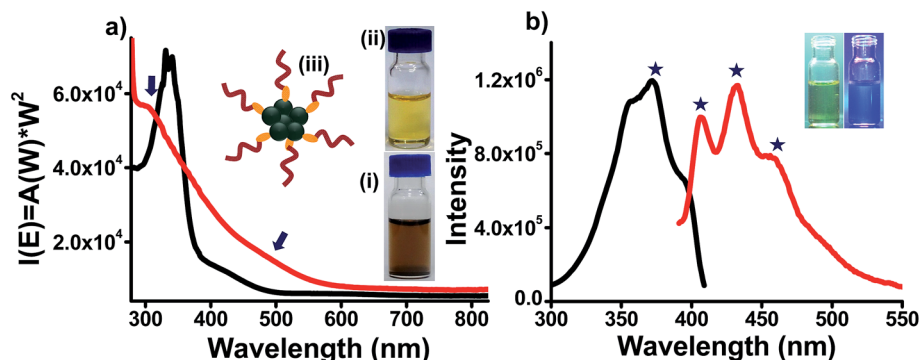
Fig. 1 (a) UV/Vis spectra of the $Ir_9(PET)_6$ in THF (red trace) and Ir–PET thiolates in ethanol (black trace). Inset shows (i) photograph of the THF solution of the cluster having greenish brown color and (ii) photograph of Ir–PET thiolates in ethanol having yellow color and (iii) is a schematic representation of the cluster (color codes: tan – Ir, orange – S and dark red – hydrocarbon chain of the thiol, in this case the phenylethyl groups), (b) photoluminescence data of the cluster. Black trace shows the excitation spectrum and red trace corresponds to the emission spectrum (excited at 370 nm) showing peaks at 404, 432 and 460 nm as indicated by asterisks. Inset shows the photographs of the cluster under visible (left) and UV (right) irradiation.
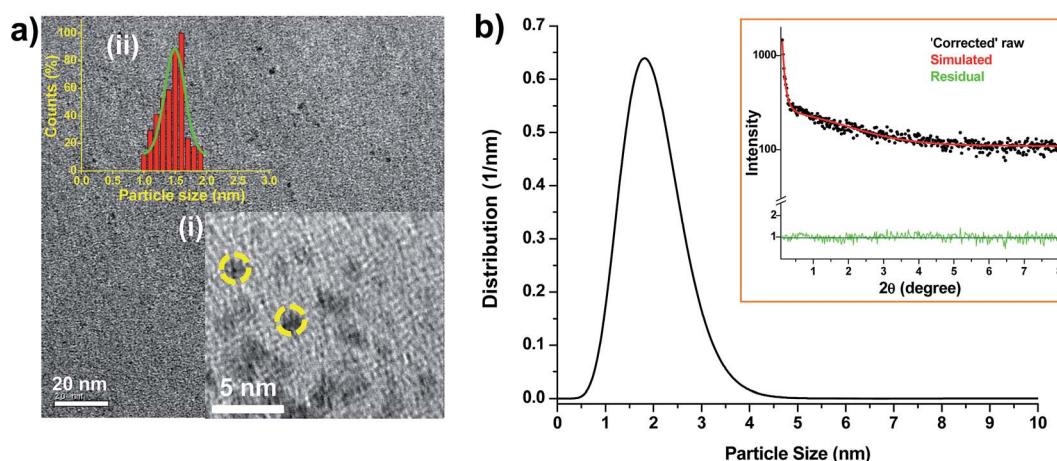
Fig. 2 (a) TEM image of $Ir_9(PET)_6$ obtained by drop casting THF solution of the cluster on a carbon-coated copper grid. A higher magnification image is shown as inset (i). Two of the particles are encircled. While the point resolution of the HRTEM was 0.12 nm, no lattice features were seen in the sample as expected. Many of the particles aggregate upon continuous irradiation and so only some of them present a true picture of the sample. Inset (ii) shows the particle size distribution obtained by counting the sizes of 50 particles manually by expanding the image. (b) Particle size distribution of the cluster obtained by SAXS analysis. The inset shows the corrected raw, simulated and residual patterns fitted by 'core–shell' model.

parameters have been given in Table S1 (see ESI†). Core–shell model reveals an average Ir core size of ~1.6 nm and particle size of ~2 nm, which agrees well with the result from the sphere model (~1.99 nm). Thus both TEM and SAXS confirmed the cluster size regime (<2 nm) of the particles.

The elemental characteristics of the cluster were determined by XPS. The survey spectrum is shown in Fig. S3 (see ESI†). As expected, Ir, S, O and C were detected. The oxidation state of Ir was confirmed to be close to 0 by the positions of the $Ir4f_{7/2}$ and $Ir4f_{5/2}$ peaks. A comparison of positions of these two peaks in $Ir_9(PET)_6$ and $IrCl_3$ is shown in Fig. 3a. The shift of $Ir4f_{7/2}$ and $Ir4f_{5/2}$ peaks to lower binding energies, 60.97 eV and 63.90 eV, respectively, as compared to 62.75 eV and 65.72 eV in $IrCl_3$ is due to the reduction of Ir from +3 to 0 oxidation state. Typical values of $Ir4f_{7/2}$ and $Ir4f_{5/2}$ are 60.90 eV and 63.88 eV,

respectively, for the metal. The Ir^{3+} positions are marked by dotted lines in the figure.

The cluster was also characterized by FT-IR spectroscopy. Comparison of the FT-IR spectra of the cluster and the free thiol is shown in Fig. 3b, which revealed that the S–H bond stretching in PET at 2560 cm^{-1} was absent in $Ir_9(PET)_6$. This indicates the loss of thiolate proton and RS–Ir bond formation in the cluster.

The cluster was also characterized by ^1H NMR spectroscopy. The NMR spectra of $Ir_9(PET)_6$ (red trace) and free thiol (black trace) along with schematic structure of the cluster and the structure of PET molecule are shown in Fig. 4. The peaks corresponding to two $-CH_2$ protons of PET anchored on the cluster surface have been severely broadened and shifted to lower ppm values as compared to the free thiol. Also $-CH_2$ protons (1) near to the cluster core are expected to be more
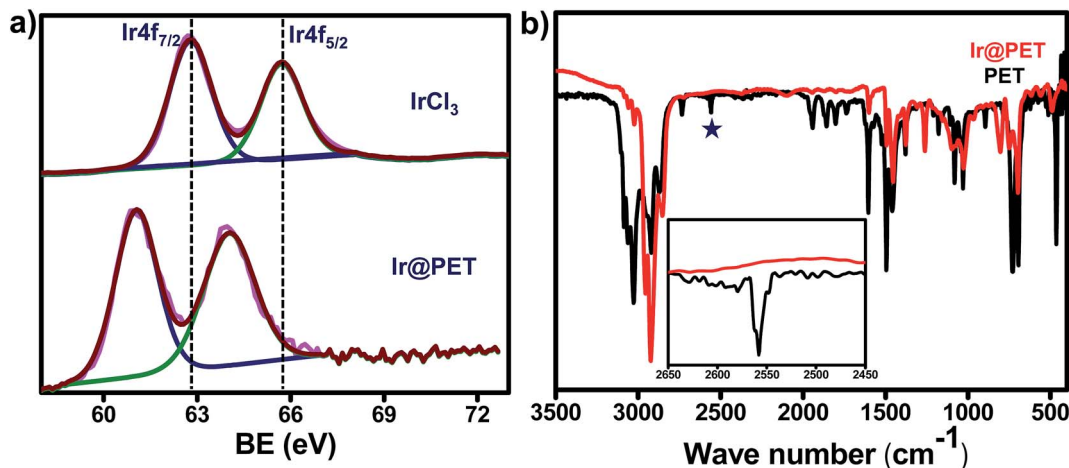
Fig. 3   (a) XPS data showing $Ir4f_{7/2}$ and $Ir4f_{5/2}$ peaks of $Ir_9(PET)_6$ compared with that of $IrCl_3$, (b) IR spectra of $Ir_9(PET)_6$ (red trace) and free PET (black trace). The peak highlighted by asterisk corresponds to S−H stretching frequency of free thiol. The S−H stretching region of the two traces is expanded separately in the inset.

effected than the other $-CH_2$ protons (2). This is expected due to the non-uniform distribution of the ligands on metal surface.[4,60,61] Based on these facts, a tentative assignment of the features is indicated. A proper assignment of all the peaks is not possible at this stage due to unavailability of the structure of the cluster. The lower ppm region of the spectra is expanded in ESI, Fig. S4.†

In ESI Fig. S5,† powder XRD pattern of $Ir_9(PET)_6$ is shown which was measured by drop casting a THF solution of the sample on a glass substrate and drying it, over and over again so as to form a thick layer. This showed weak and broad signals corresponding to (111) and (220) planes of Ir. The broad peaks are an indication of the nano size regime of the particles.

Dass *et al.* have revealed through their study of MALDI TOF mass spectrometry of $Au_{25}(SR)_{18}$ cluster that the choice of the matrix plays an important role in getting intact molecular ion

Fig. 4   NMR spectra of $Ir_9(PET)_6$ (red trace) and free PET (black trace) measured in $CDCl_3$. The schematic structure of the cluster and the structure of PET are shown. The assignments are indicated. The label, * indicate unassigned features.

peaks without fragmentation.[62] Since this cluster is a new system, we performed MALDI MS measurements using various commonly used matrices like *trans*-2-[3-(4-*tert*-butylphenyl)-2-methyl-2-propenylicene malanonitrile (DCTB), 2,5-dihydroxybenzoic acid (DHB), sinapinic acid (SA) and 2-cyano-4-hydroxy cinnamic acid (CHCA). The mass spectra (Fig. S6, ESI†) obtained using DCTB and CHCA contained a bunch of peaks due to fragmentation and it was difficult to obtain any information on the cluster composition using them. In contrast, the mass spectrum using the SA did not yield any peak. Only DHB gave a good mass spectrum with well-defined peaks and was therefore chosen for the further analysis. This is unlike the case of Au and Ag clusters where DCTB is usually used as a matrix for MALDI MS analysis and is known to give good results.

Fig. 5 shows the MALDI MS results of the cluster measured in the linear positive mode using the DHB matrix. The highest intensity molecular ion peak can be assigned to the $[Ir_9(PET)_6]^+$ ion. The observed spectrum for $[Ir_9(PET)_6]^+$ is in good agreement with the calculated spectrum as shown in inset (i) of Fig. 5 and S7 in ESI.† The peak with the next highest intensity is assigned to $[Ir_8(PET)_4]^+$ species. To check whether it is a fragment obtained due to laser during measurement or indeed present in the solution, a laser intensity dependent MALDI MS study was performed. These spectra measured in the linear positive mode are shown as inset (iii) of Fig. 5. The $[Ir_8(PET)_4]^+$ peak was not present at the lowest laser energy where the molecular ion peak was observed. But with increase in laser power, both the peaks increase in intensity linearly. Hence, we conclude that this species is not a fragment.

The stability of the cluster solution in THF was checked by time dependent UV/Vis spectra measurement. For this purpose two set of cluster solutions in THF were synthesized. One sample was stored in fridge (at ∼4 °C) and another at room temperature. UV/Vis spectra of both the samples were recorded each day up to a time period of 7 days which are shown in Fig. S8 (in ESI).† We observed no change in UV/Vis spectrum of sample stored in fridge up to 7 days confirming it is stable over this
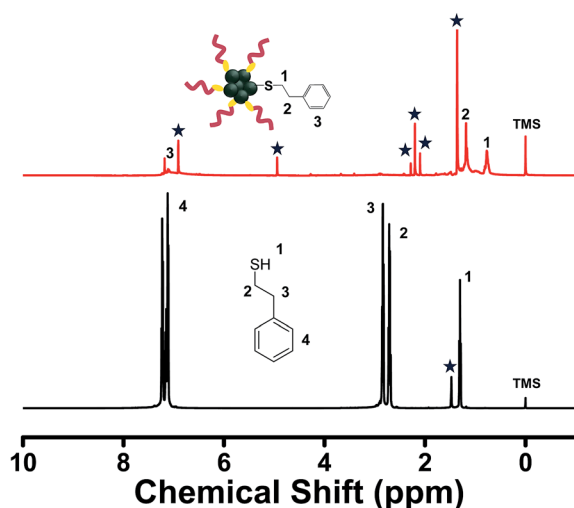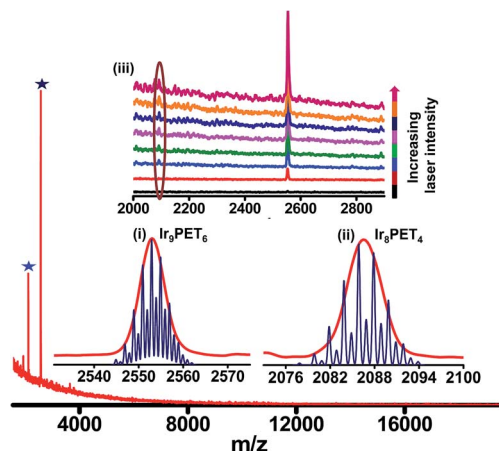
Fig. 5 MALDI MS of the cluster measured in the linear positive mode using DHB as the matrix. The highest intensity peak (highlighted by navy blue asterisk) is assigned to $Ir_9(PET)_6$. Inset (i) shows the observed (red trace) and calculated (blue trace) spectra of $[Ir_9(PET)_6]^+$ species. The next highest intensity peak (highlighted by blue asterisk) is assigned to $Ir_8(PET)_4$ and its observed (red trace) and calculated (blue trace) spectra are shown in inset (ii). Inset (iii) shows the laser intensity dependent MALDI MS of the cluster measured in linear positive mode. The increasing order of laser energy used to measure each spectrum is indicated on the right side.

Fig. 6 Optimized geometries of structural isomers of (a–i) $Ir_3(SCH_3)_2$. H, C, S and Ir atoms are represented as green, brown, yellow and purple spheres. The relative energies (in eV) of the structural isomers are given in {}. The three most stable isomers are highlighted by red lines. The calculated S–C vibrational frequencies (cm^{-1}) are also listed for each isomer.

period. Whereas sample stored at room temperature was stable up to 2 days.

The aim of our DFT computations is to use simple model systems to develop an insight on how the ligands may prefer to arrange in the comparatively larger $Ir_9(PET)_6$ cluster. In order to take into account ligand–ligand interactions, we first examined several structural isomers of $Ir_3(SCH_3)_2$. These are displayed in Fig. 6 along with their relative energies. The three most stable isomers are (d), (i) and (b). In (d) the three Ir atoms are bonded to form a triangle and both the SCH_3 ligands are shared between two Ir atoms. In (i) the three Ir atoms are bonded to form a triangle, one SCH_3 ligand is shared between two Ir atoms while the second ligand is singly attached. In (b) one pair of Ir atoms is non-bonded with one SCH_3 ligand shared between them and the second ligand is singly attached to the third Ir atom. The most unfavourable isomer is (a) comprising of two pairs of non-bonded Ir atoms, with each pair sharing a ligand between them in a ring-like fashion. The relative energies of isomers (d), (i) and (b) are within 0–0.05 eV and of the other structures are >0.13 eV. Thus, we expect Ir–PET–Ir arrangements in the $Ir_9(PET)_6$ cluster of the form in isomers (d), (i) or (b). However, such structural differences would be reflected in their IR and NMR spectra, which can then be used as identifying features. IR and NMR spectroscopies have been used as important techniques to understand structure and chemical composition of MPC monolayers.[4] DFT calculations of IR spectra of bare clusters of Ir[63] and NMR chemical shifts for certain Ir complexes[64] are also known.

The position of the S–C vibrational peak for each structural isomer of $Ir_3(SCH_3)_2$ obtained from DFT calculated IR spectra are also shown in Fig. 6. It is noticeable that if all the ligands were structurally equivalent, then only a single peak for the S–C
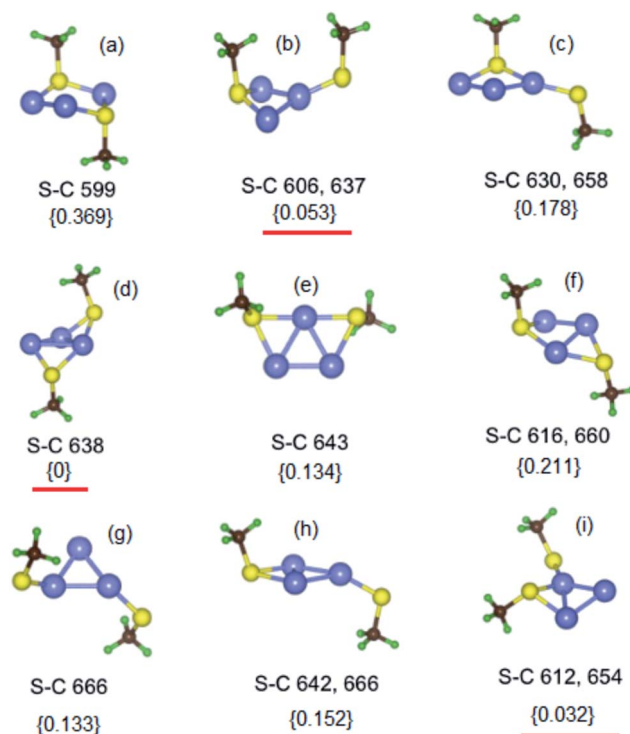
vibration would appear, as in case of isomers (a), (d), (g) and (e). When SCH_3 ligands are present in two types of arrangements, then depending upon their nearness, which determines the ligand–ligand interaction, the effect on the S–C peak is different. Isomers (b) and (g) where the two SCH_3 ligands are separated by an Ir–Ir bond, the two S–C peaks are seen at similar positions in the isomers with equivalent ligands. For instance, in isomers (3) and (g), the S–C peak occurs at 643 and 666 cm^{-1}, respectively and in isomer (h) two peaks are observed at 642 and 666 cm^{-1}. But if the two ligands share an Ir atom, then one of the S–C peaks is strongly shifted as in the case of isomers (c), (f) and (i). Elaborating the S–C peaks which are seen at ~640 cm^{-1} for isomers (d) and (e) and at 666 cm^{-1} for isomer (g) are shifted to 612 and 654 cm^{-1} for isomer (i). Overall, irrespective of the ligand–ligand interaction strength, if the ligands are differently arranged, then two distinct S–C peaks arise with a separation of ~25–40 cm^{-1}.

Fig. 7 illustrates the DFT calculated IR spectra of the three structural isomers (j)–(l) of $Ir_3(PET)_1$. The relative energies exhibit that the most stable structure is (l) in which the PET ligand is shared between bonded Ir atoms. The most unfavored geometry is (j) in which the PET ligand is shared between two non-bonded Ir atoms. Depending on whether the PET ligand is shared between non-bonded Ir atoms (isomer j), shared between bonded Ir atoms (isomer l), or singly attached to an Ir atom (isomer k), the position of the S–C vibrational peak is
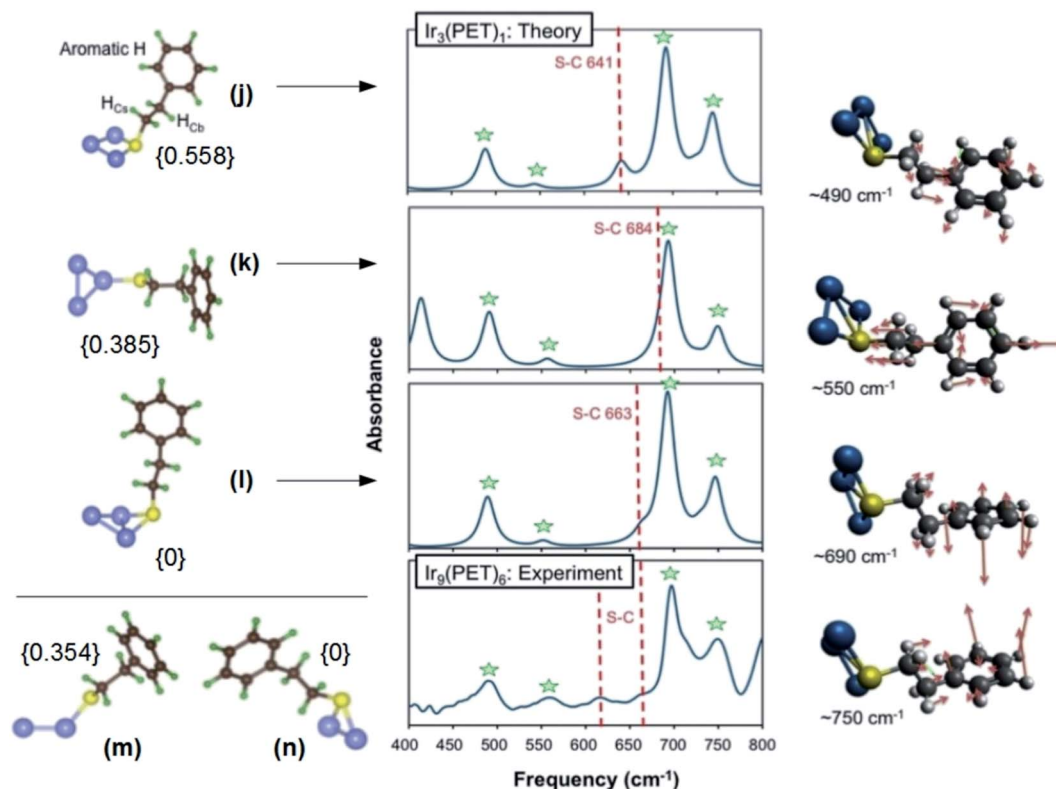
Fig. 7 Geometries of the structural isomers of $Ir_3(PET)_1$ (j–l) and $Ir_2(PET)_1$ (m and n) are depicted in the first column. The relative energies (in eV) are given in {}. In the second column theoretically (DFT) computed IR spectra (top three panels) of isomers (j–l) are compared with the experimental IR spectrum of $Ir_9(PET)_6$ (bottom panel). The common features exhibited are highlighted as stars and the corresponding vibrational modes are shown in the third column for isomer (j). The red arrows are the force vectors on the atoms participating in the vibration.

distinct and is found at 641, 663 and 684 cm^{-1}, respectively. The same order of appearance of the S–C peak is observed for the $Ir_3(SCH_3)_2$ isomers (a) (599 cm^{-1}), (d) (640 cm^{-1}) and (g) (666 cm^{-1}) (see Fig. 6). The experimentally obtained IR spectrum of $Ir_9(PET)_6$, expanded in the 400–800 cm^{-1} region is also presented in Fig. 7. It exhibits several peaks (marked as stars) in common for all the model clusters. This remarkable correlation suggests that spectra computed in other regions may be true representations of the structure.

These common features are assigned to the vibrational modes also displayed in the figure for the specific case of isomer (j) of $Ir_3(PET)_1$. Most importantly, two clear peaks at ~620 and 660 cm^{-1} are observed, suggesting that there are two different arrangements of the PET ligands in the structure of $Ir_9(PET)_6$. Based on the variation of S–C vibrational peaks for $Ir_3(SCH_3)_2$ isomers in Fig. 6, we believe that the structural arrangement of the ligands in the synthesized $Ir_9(PET)_6$ cluster may be similar to that in isomer (i) in which both the peaks are shifted to relatively lower frequencies than isomers (d) and (g).

^{1}H NMR chemical shifts (δ) are highly affected by the chemical environment. We present the calculated atomic charges over selected $Ir_3(SCH_3)_2$ structural isomers in Table 1. Recalling from Fig. 6, the two SCH_3 ligands are symmetrically arranged in isomers (a), (d) and (g). Consequently the charges on each pair of S and C atoms are calculated to be the same within these isomers as opposed to isomers (b) and (f) in which

the two ligands are inequivalent. Therefore, we would expect to see shifting of each of the two CH_2 proton peaks to two specific positions in the experimental ^{1}H NMR spectrum of the $Ir_9(PET)_6$ cluster relative to PET. However, this is not the case and several peaks are found in Fig. 4 and ESI, Fig. S4† which are down-shifted to lower δ values. This suggests that all the ligands in the synthesized cluster are not structurally and therefore, chemically equivalent.

In this work we have chosen to compute the δ values (in ppm) of PET ligand, $Ir_2(PET)_1$ and $Ir_3(PET)_1$ clusters instead of Ir–SCH_3 clusters. These are also listed in Table 1 along with the ^{1}H NMR chemical shifts of the PET ligand and the cluster from experiments. As discussed earlier and can be noticed from the table, experimentally the δs of H atoms (H_{C_b} and H_{C_s}) belonging to the benzylic C atom (C_b) and C atom near S (C_s) move to lower values relative to the PET ligand on cluster formation. The C and H atoms are referred by the labelling shown in isomer (j) in Fig. 7. Our primary objectives are to (i) determine whether such trends are reflected in the abovementioned model cluster systems that we have considered herein and (ii) develop an understanding of the changes in electronic structure leading to these shifts.

Table 1 shows that for certain geometrical arrangements of the clusters (isomers (m), (j) and (l) in Fig. 7) a decrease in δ is predicted relative to the PET ligand in agreement with the experiments. To explain the NMR chemical shift trends we

Table 1 ^{1}H NMR chemical shifts (in ppm) of aromatic H atoms, H atoms in benzylic CH_2 (H_{C_b}) and H atoms in CH_2 bonded to S (H_{C_s}) in PET and Ir@PET clusters from DFT calculations and experiments. Atomic charges over benzylic C (C_b), C bonded to S (C_s), S, and Ir atoms in Ir@PET (Fig. 7) and Ir@SCH$_3$ (Fig. 6) clusters depicted in Fig. 7 are also listed. The above mentioned labelling of atoms can be seen in Fig. 7

		Chemical shift (ppm)			
Method	System	Aromatic H	H_{C_b}	H_{C_s}	SH
Calculation	PET	7.63–7.64	3.04	3.14	2.37
	Ir$_2$(PET)$_1$ (iso. (m))	7.47–7.73	2.61, 2.93	0.76, 1.88	
	Ir$_2$(PET)$_1$ (iso. (n))	7.52–7.85	2.94, 3.74	3.73, 4.19	
	Ir$_3$(PET)$_1$ (iso. (j))	7.52–7.90	1.96, 5.65	3.97, 9.18	
	Ir$_3$(PET)$_1$ (iso. (k))	7.48–7.56	3.95	3.10	
	Ir$_3$(PET)$_1$ (iso. (l))	7.24–7.62	1.90, 3.03	2.62, 3.23	
Experiment	PET	7.11–7.24	2.82–2.86	2.73–2.66	1.29–1.32
	Ir$_9$(PET)$_6$	6.91–7.23	2.09–2.28	0.76–1.36	

		Atomic charges $(e)^a$					
System	Isomer	C_b	C_s	S	Ir$_1$	Ir$_2$	Ir$_3$
PET		0.07	0.18	−0.15			
Ir$_2$(PET)$_1$	Iso. (m)	0.10	0.11	−0.20	0.16	−0.06	
	Iso. (n)	0.04	0.00	0.27	−0.15	−0.13	
Ir$_3$(PET)$_1$	Iso. (j)	0.03	−0.03	0.12	−0.17	−0.14	0.19
	Iso. (k)	0.11	0.18	−0.30	0.14	−0.01	−0.01
	Iso. (l)	0.05	0.07	0.03	0.00	0.02	−0.14
Ir$_3$(SCH$_3$)$_2$	Iso. (a)		−0.15, −0.15	−0.16, −0.16	0.03	0.03	0.03
	Iso. (d)		−0.12, −0.12	−0.32, −0.32	0.23	0.04	0.08
	Iso. (g)		−0.15, −0.15	−0.24, −0.24	0.12	0.12	−0.05
	Iso. (b)		−0.15, −0.18	−0.16, −0.25	0.03	0.03	0.12

^{a} Atomic charges over PET and Ir@PET clusters are calculated from APT analysis and atomic charges over Ir@SCH$_3$ clusters are from Mulliken population analysis scheme.

analysed the atomic charges which are also listed in Table 1. In PET ligand and the clusters, the aromatic H atoms are the least shielded from the magnetic field and so are found at significantly large δ values ($\sim$7 ppm). In comparison the S atom in PET is electronegative with $-0.15e$ charge and its high electron density shields the H atom (directly bonded to it) from the magnetic field and consequently the proton exhibits a low δ value. C_b and C_s are positively charged ($C_b < C_s$) and so the corresponding H_{C_b} and H_{C_s} exhibit medium chemical shifts $\sim$3 ppm ($H_{C_b} < H_{C_s}$).

In isomer (m) of Ir$_2$(PET)$_1$, in which PET is singly attached, charge transfer from the Ir atoms makes S more negative. However, the magnitude of net charge on S available for interaction with C_s is reduced. Consequently, the positive charge on C_s is also reduced and a decrease in δ of H_{C_s} atom occurs. In contrast the positive charge on C_b is increased and while we expect δ of H_{C_s} to increase, a slight decrease is predicted from the calculations. In the analogous isomer (k) of Ir$_3$(PET)$_1$ the positive charge on C_s is unchanged and on C_b is slightly increased compared to in PET. As a result δ of H_{C_s} and H_{C_b} is similar and increased, respectively with respect to PET. It is interesting to note that though in both isomers (m) and (k) the ligand is singly attached, the former exhibits chemical shifts in better agreement with experiments. We speculate that this could be due to more effective shielding of the magnetic field by the increased charge density over S atom in isomer (m) than in

isomer (k). In isomer (n) of Ir$_2$(PET)$_1$ the scenario is opposite: the atomic charge of S becomes positive ($+0.27e$) and it supersedes the increase in electron density over the C atoms, such that the CH_2 protons exhibit an increased chemical shift with respect to in PET. Comparatively, in isomer (l) of Ir$_3$(PET)$_1$ the S atom has a small positive charge and the positive charges over C_s and C_b are reduced (vs. PET) implying an increased electron density which shields the attached H_s and decreases their chemical shifts. The S atom in isomer (j) of Ir$_3$(PET)$_1$ has a reasonable positive charge (0.12) and only one of the H_{C_b} atoms exhibits a decreased chemical shifts while the other H_{C_b} and H_{C_s} protons show significantly increased δ which is not observed in the experimental NMR. Thus, we believe that in Ir$_9$(PET)$_6$, some PET ligands are attached to a single Ir atom and others are shared by a pair of bonded Ir atoms.

5. Conclusion and summary

In summary, we report an atomically precise Ir cluster protected by 2-phenylethanethiol ligand, which was synthesized following a solid state synthetic protocol and whose composition was determined based on MALDI MS studies. Characterization using various other techniques also supports its formation. Comparison of experimental spectroscopic data with the theoretical predictions suggests two types of ligands, one directly linking the metal and another bridging the metal, in the

structure. Efforts are on-going to crystallize the cluster which will give further insight into its structure. We believe that this cluster may find important applications in catalysis and this report may encourage further investigations in the area of protected Ir clusters.

Acknowledgements

References

1 Y. Lu and W. Chen, *Chem. Soc. Rev.*, 2012, **41**, 3594–3623.

2 J. P. Wilcoxon and B. L. Abrams, *Chem. Soc. Rev.*, 2006, **35**, 1162–1194.

3 M. Brust, M. Walker, D. Bethell, D. J. Schiffrin and R. Whyman, *J. Chem. Soc., Chem. Commun.*, 1994, 801–802, DOI: 10.1039/c39940000801.

4 A. C. Templeton, W. P. Wuelfing and R. W. Murray, *Acc. Chem. Res.*, 2000, **33**, 27–36.

5 A. Mathew and T. Pradeep, *Part. Part. Syst. Charact.*, 2014, **31**, 1017–1053.

6 T. Udayabhaskararao and T. Pradeep, *J. Phys. Chem. Lett.*, 2013, **4**, 1553–1564.

7 R. Jin, *Nanoscale*, 2010, **2**, 343–362.

8 H. Qian, M. Zhu, Z. Wu and R. Jin, *Acc. Chem. Res.*, 2012, **45**, 1470–1479.

9 P. Maity, S. Xie, M. Yamauchi and T. Tsukuda, *Nanoscale*, 2012, **4**, 4027–4037.

10 T. U. B. Rao, B. Nataraju and T. Pradeep, *J. Am. Chem. Soc.*, 2010, **132**, 16304–16307.

11 I. Chakraborty, W. Kurashige, K. Kanehira, L. Gell, H. Hakkinen, Y. Negishi and T. Pradeep, *J. Phys. Chem. Lett.*, 2013, **4**, 3351–3355.

12 I. Chakraborty, A. Govindarajan, J. Erusappan, A. Ghosh, T. Pradeep, B. Yoon, R. L. Whetten and U. Landman, *Nano Lett.*, 2012, **12**, 5861–5866.

13 C. P. Joshi, M. S. Bootharaju, M. J. Alhilaly and O. M. Bakr, *J. Am. Chem. Soc.*, 2015, **137**, 11578–11581.

14 L. Liao, S. Zhou, Y. Dai, L. Liu, C. Yao, C. Fu, J. Yang and Z. Wu, *J. Am. Chem. Soc.*, 2015, **137**, 9511–9514.

15 S. Wang, Y. Song, S. Jin, X. Liu, J. Zhang, Y. Pei, X. Meng, M. Chen, P. Li and M. Zhu, *J. Am. Chem. Soc.*, 2015, **137**, 4018–4021.

16 X. Jia, J. Li, L. Han, J. Ren, X. Yang and E. Wang, *ACS Nano*, 2012, **6**, 3311–3317.

17 N. Goswami, A. Giri, M. S. Bootharaju, P. L. Xavier, T. Pradeep and S. K. Pal, *Anal. Chem.*, 2011, **83**, 9676–9680.

18 R. Ghosh, A. K. Sahoo, S. S. Ghosh, A. Paul and A. Chattopadhyay, *ACS Appl. Mater. Interfaces*, 2014, **6**, 3822–3828.

19 K. Salorinne, X. Chen, R. W. Troff, M. Nissinen and H. Haekkinen, *Nanoscale*, 2012, **4**, 4095–4098.

20 A. Ganguly, I. Chakraborty, T. Udayabhaskararao and T. Pradeep, *J. Nanopart. Res.*, 2013, **15**, 1522.

21 S.-i. Tanaka, J. Miyazaki, D. K. Tiwari, T. Jin and Y. Inouye, *Angew. Chem., Int. Ed.*, 2011, **50**, 431–435.

22 X. Huang, B. Li, L. Li, H. Zhang, I. Majeed, I. Hussain and B. Tan, *J. Phys. Chem. C*, 2012, **116**, 448–455.

23 X. Le Guevel, V. Trouillet, C. Spies, G. Jung and M. Schneider, *J. Phys. Chem. C*, 2012, **116**, 6047–6051.

24 I. Chakraborty, R. G. Bhuin, S. Bhat and T. Pradeep, *Nanoscale*, 2014, **6**, 8561–8564.

25 H. Erdogan, O. Metin and S. Oezkar, *Phys. Chem. Chem. Phys.*, 2009, **11**, 10519–10525.

26 M. Hyotanishi, Y. Isomura, H. Yamamoto, H. Kawasaki and Y. Obora, *Chem. Commun.*, 2011, **47**, 5750–5752.

27 S. Nassreddine, G. Bergeret, B. Jouguet, C. Geantet and L. Piccolo, *Phys. Chem. Chem. Phys.*, 2010, **12**, 7812–7820.

28 M. Rueping, R. M. Koenigs, R. Borrmann, J. Zoller, T. E. Weirich and J. Mayer, *Chem. Mater.*, 2011, **23**, 2008–2010.

29 Z. Xu, F. S. Xiao, S. K. Purnell, O. Alexeev, S. Kawi, S. E. Deutsch and B. C. Gates, *Nature*, 1994, **372**, 346–348.

30 A. Berko and F. Solymosi, *Surf. Sci.*, 1998, **411**, L900–L903.

31 A. M. Argo, J. F. Odzak and B. C. Gates, *J. Am. Chem. Soc.*, 2003, **125**, 7107–7115.

32 A. M. Argo, J. F. Odzak, J. F. Goellner, F. S. Lai, F. S. Xiao and B. C. Gates, *J. Phys. Chem. B*, 2006, **110**, 1775–1786.

33 C. Aydin, J. Lu, M. Shirai, N. D. Browning and B. C. Gates, *ACS Catal.*, 2011, **1**, 1613–1620.

34 C. Kerpal, D. J. Harding, G. Meijer and A. Fielicke, *Eur. Phys. J. D*, 2011, **63**, 231–234.

35 V. S. Garcia-Cuello, L. Giraldo and J. C. Moreno-Pirajan, *Catal. Lett.*, 2011, **141**, 1659–1669.

36 J. Dupont, G. S. Fonseca, A. P. Umpierre, P. F. P. Fichtner and S. R. Teixeira, *J. Am. Chem. Soc.*, 2002, **124**, 4228–4229.

37 G. S. Fonseca, A. P. Umpierre, P. F. P. Fichtner, S. R. Teixeira and J. Dupont, *Chem.–Eur. J.*, 2003, **9**, 3263–3269.

38 E. Bayram, M. Zahmakıran, S. Özkar and R. G. Finke, *Langmuir*, 2010, **26**, 12455–12464.

39 C. K. Yee, R. Jordan, A. Ulman, H. White, A. King, M. Rafailovich and J. Sokolov, *Langmuir*, 1999, **15**, 3486–3491.

40 R. Redon, F. Ramirez-Crescencio and A. L. Fernandez-Osorio, *J. Nanopart. Res.*, 2011, **13**, 5959–5965.

41 M.-H. So, C.-M. Ho, R. Chen and C.-M. Che, *Chem.–Asian J.*, 2010, **5**, 1322–1331.

42 T. Zhang, S.-C. Li, W. Zhu, J. Ke, J.-W. Yu, Z.-P. Zhang, L.-X. Dai, J. Gu and Y.-W. Zhang, *Surf. Sci.*, 2016, **648**, 319–327.

43 R. Vankayala, G. Gollavelli and B. K. Mandal, *J. Mater. Sci.: Mater. Med.*, 2013, **24**, 1993–2000.

44 D. J. Gavia, Y. Do, J. Gu and Y.-S. Shon, *J. Phys. Chem. C*, 2014, **118**, 14548–14554.

45 Y. Zhu, H. Qian, B. A. Drake and R. Jin, *Angew. Chem., Int. Ed.*, 2010, **49**, 1295–1298.

46 M. J. Frish, G. W. Trucks, H. B. Schlegel, G. E. Scuseria, M. A. Robb, J. R. Cheeseman, G. Scalmani, V. Barone, B. Mennucci and G. A. Petersson, *et al.*, *Gaussian 09*, Gaussian, Inc., Wallingford CT, 2009.

47 W. Bouderbala, A.-G. Boudjahem and A. Soltani, *Mol. Phys.*, 2014, **112**, 1789–1798.

48 M. Zhang and R. Fournier, *Phys. Rev. A: At., Mol., Opt. Phys.*, 2009, **79**, 043203.

49 S. A. Aravindh, *Appl. Nanosci.*, 2014, **4**, 593–600.

50 J. B. A. Davis, S. L. Horswell and R. L. Johnston, *J. Phys. Chem. A*, 2014, **118**, 208–214.

51 F. Weigend and R. Ahlrichs, *Phys. Chem. Chem. Phys.*, 2005, **7**, 3297–3305.

52 F. Weigend, *Phys. Chem. Chem. Phys.*, 2006, **8**, 1057–1065.

53 J. Cioslowski, *J. Am. Chem. Soc.*, 1989, **111**, 8333–8336.

54 G. Schaftenaar and J. H. Noordik, *J. Comput.-Aided Mol. Des.*, 2000, **14**, 123–134.

55 T. A. Keith and R. F. W. Bader, *Chem. Phys. Lett.*, 1992, **194**, 1–8.

56 T. A. Keith and R. F. W. Bader, *Chem. Phys. Lett.*, 1993, **210**, 223–231.

57 J. A. Creighton and D. G. Eadon, *J. Chem. Soc., Faraday Trans.*, 1991, **87**, 3881–3891.

58 A. Baksi, A. Mitra, J. S. Mohanty, H. Lee, G. De and T. Pradeep, *J. Phys. Chem. C*, 2015, **119**, 2148–2157.

59 A. Mitra and G. De, *Langmuir*, 2014, **30**, 15292–15300.

60 M. Habeeb Muhammed, S. Ramesh, S. Sinha, S. Pal and T. Pradeep, *Nano Res.*, 2008, **1**, 333–340.

61 T. G. Schaaff, M. N. Shafigullin, J. T. Khoury, I. Vezmar and R. L. Whetten, *J. Phys. Chem. B*, 2001, **105**, 8785–8796.

62 A. Dass, A. Stevenson, G. R. Dubay, J. B. Tracy and R. W. Murray, *J. Am. Chem. Soc.*, 2008, **130**, 5940–5946.

63 J.-G. Du, X.-Y. Sun, J. Chen and G. Jiang, *J. Phys. Chem. A*, 2010, **114**, 12825–12833.

64 J. Vicha, M. Patzschke and R. Marek, *Phys. Chem. Chem. Phys.*, 2013, **15**, 7740–7754.